2017

Tip-enhanced Raman scattering of graphene

Ryan Beams
National Institute of Standards and Technology, ryan.beams@nist.gov

Review

Journal of RAMAN SPECTROSCOPY

Received: 28 March 2017 Revised: 19 June 2017 Accepted: 20 June 2017 Published online in Wiley Online Library

(wileyonlinelibrary.com) DOI 10.1002/jrs.5211

Tip-enhanced Raman scattering of graphene

Ryan Beams*

This article reviews the mechanism of tip-enhanced Raman spectroscopy (TERS) and its importance for characterizing graphene. The theoretical foundation of TERS and experimental implementation are discussed. Conventionally, Raman scattering is treated as a spatially incoherent process where the total signal is proportional to the scattering volume. However, in the near-field regime, the scattered fields can add coherently because the TERS interaction volume is on the same length scale as the phonon correlation length. These coherence effects are significant for two-dimensional materials as will be discussed theoretically and experimentally. Therefore, TERS provides an optical method to probe phonon correlations at the nanoscale. In addition, this article will review the TERS applications for characterizing defects, edges, and nanoscale strain in graphene. Finally, the outlook and future applications are discussed. Published 2017. This article is a U.S. Government work and is in the public domain in the USA.

Keywords: TERS; near-field microscopy; graphene; defects; edges

Introduction

Raman spectroscopy is extensively used in characterizing the properties of graphene and the quality of graphene-based devices. This has been due in large part to the sensitivity of Raman scattering to structural and chemical properties. While Raman spectroscopy measurements are common in a wide range of organic and condensed matter systems, it is a particularly powerful technique for graphitic systems and is often implemented to measure defect density,[1,2] strain,[3–8] and electro-static doping.[9] Pristine graphene is characterized by two main Raman features: the G band ($\approx$1580 cm^{-1}) and the G′ or 2D band ($\approx$2700 cm^{-1}); this work the latter peak will be referred to as the G′ peak because 2D will be used for two-dimensional. The G band is a doubly degenerate first-order feature belonging to the E_{2g} irreducible representation.[10] This mode is a C-C stretch and is present in all sp^2 carbon systems. The strongest feature in graphene is the G′ band, which is a second-order in-plane breathing mode and belongs to the A_1 irreducible representation.[10] The lineshape of the G′ band is commonly used to determine the number of graphene layers as well as the stacking order.[11–13] The position and widths of the G and G′ bands also characterize the electro-static doping[9] and mechanical strain.[3–8]

Another band that is frequently used to characterize graphene is the disorder-induced D band ($\approx$1350 cm^{-1}). It has the same mode symmetry as the G′ band, but the momentum conservation is fulfilled by the electron-hole pair scattering off a defect instead of a second phonon. Because a defect is required for the D band activation, it is not detectable in pristine graphene crystals and is used to quantitatively determine the defect density as well as the type of defects present in the sample.[1,2,14,15] One important class of defects in graphene is edges, which behave as line defects by breaking the translational symmetry of the crystal lattice.[16–18] The Raman process in graphene is discussed in detail in several review articles.[10,19–22]

While the Raman studies of graphene have provided a detailed understanding of the physical properties of the material, the limited spatial resolution of conventional Raman spectroscopy is insufficient to study material properties at the nanoscale. As the footprint of devices continues to decrease, characterization at the nanometer scale becomes crucial. Furthermore, because the conventional Raman signal scales with the scattering volume, far-field superresolution techniques are impracticable for nanoscale Raman spectroscopy because of the signal strength.[23,24] Both of these limitations can be overcome with tip-enhanced Raman spectroscopy (TERS), which allows for high spatial resolution imaging by locally enhancing the excitation and scattered fields. For graphene, TERS has allowed for nanoscale imaging of twisted bilayer graphene,[25] characterization of the number of graphene layers,[26–28] surface contamination,[29,30] defects and edges,[29,31–34] strain,[35–38] doping,[39] and plasmonic effects.[40].

In this article, the principles and applications of TERS for graphene are reviewed. The theoretical basis for the TERS process in graphene is discussed in the Tip-enhanced Raman Scattering section, including discussing the origin of the TERS signal and the scattering terms. The experimental implementation is presented in the Experimental Setup section. Applications of TERS of graphene including the theoretical formalism and measurements of the spatial correlations of phonons (Coherence Effects section), the characterization of defects and edges (Section on TERS Characterization of Edges and Defects section), and the measurement of local strain (Strain section) are discussed. Finally, the outlook for TERS in graphene and other 2D materials.

Tip-enhanced Raman scattering

The diffraction limit

While optical measurements provide powerful insights into material properties, the spatial resolution is limited by diffraction and fundamentally restricts the applications for nanoscale studies.

*Correspondence to: Ryan Beams, National Institute of Standards and Technology, Gaithersburg, MD, USA.
E-mail: ryan.beams@nist.gov

National Institute of Standards and Technology, Gaithersburg, MD, USA

This issue is of increasing concern because of the ongoing miniaturization of devices and transistor gate-lengths. To understand this limitation, optical systems can be thought of as a low-pass filter for spatial frequencies with the filter edge being determined by the numerical aperture, NA $= n \sin\theta$, of the collecting lens, where n is the refractive index and θ is the half angle of the microscope objective. This limitation is generally referred to as the diffraction limit. For axially symmetric optical systems focusing plane waves, the full-width-at-half-maximum of the resulting focus is $\Delta x = 0.51\lambda/\mathrm{NA}$, where λ is the wavelength of the measured light, which gives a spatial resolution of a few hundred nanometers in the visible. This limitation has been circumvented for fluorescence samples by exploiting specific sample properties, such as saturation, photo-bleaching, and photo-switching in superresolution techniques such as stimulated emission depletion microscopy,[41] photo-activated localization microscopy,[42] and stochastic optical reconstruction microscopy.[43] However, these approaches are generally not suitable for nonfluorescent processes such as Raman. While there are proposals to adapt stimulated emission depletion-type superresoluiton approaches for Raman scattering,[44–46] these measurements will be limited by the signal-to-noise ratio at the nanoscale because far-field signal scales linearly with the scattering volume.[23,24]

The maximum resolution for a conventional optical system is achieved by collecting the entire half-sphere (NA $= n \sin\frac{\pi}{2}$) as can be seen by inspecting the definition of NA. As stated previously, this case is still insufficient for nanoscale optical measurements, which can be understood by considering the angular spectrum representation. In this representation, a monochromatic electric field at the sample, $\hat{E}(k_x, k_y; z = 0)$, can be propagated to an arbitrary image plane using a 2D Fourier transform multiplied by the propagation term, $e^{\pm ik_z z}$. The electric field, $E(x, y, z)$, in the image plane is then expressed as

$$E(x,y,z) = \int\int_{-\infty}^{\infty} \hat{E}(k_x,k_y;z=0)e^{i(k_x x+k_y y)}e^{\pm ik_z z}dk_x dk_y \qquad (1)$$

The wave vector components (k_x, k_y, k_z) are related by $k_z = \sqrt{2\pi n/\lambda - k_x^2 - k_y^2}$. This relationship shows that k_z is real valued for $2\pi n/\lambda \geq k_x^2 + k_y^2$ and imaginary for $2\pi n/\lambda < k_x^2 + k_y^2$. Therefore, the electric field propagates in z-direction ($e^{\pm ik_z z}$) for spatial frequencies below $2\pi n/\lambda \geq k_x^2 + k_y^2$ and exponentially decays for $2\pi n/\lambda < k_x^2 + k_y^2$. In other words, high spatial frequencies do not propagate away from the source. The region away from the sample that is dominated by the propagating fields from the source is referred to as the far-field, while the region close to the source containing the non-propagating evanescent fields is known as the near-field. It is important to note that far-field superresolution techniques do not increase the signal because the evanescent fields do not propagate to the far-field, which poses significant limitation for detecting signals from nanometer sources.

TERS concept

The resolution and signal limitations of conventional far-field microscopy can be overcome by detecting the near-field electric field components of the source. While there are a variety of methods to accomplish this task, the most common method utilizes a sharp metal tip in close proximity to the source to scatter the near-field components into propagating fields that can be detected in the far-field. In this case, the optical resolution is defined by the metal tip as opposed to the excitation wavelength, which means the optical resolution is a fabrication challenge opposed to a fundamental limitation as in conventional microscopy. Moreover, the tip serves to both increase the excitation field strength by localizing the field and enhance the signal by scattering out the near-field from the sample.

Because the tip scatters the near-field into the far-field, the near-field components are mixed with the far-field components. This challenge is overcome by ensuring that the enhancement is significant enough for the near-field components to dominate. However, there are many scattering terms present, which can be expressed as an infinite series as depicted in Fig. 1. The lowest order term is the interaction of the excitation field with the sample (**S**), which is the conventional far-field Raman signal. In the presence of the tip, the excitation field can also induce surface plasmon oscillations in the metal tip. The induced surface plasmons cause a secondary field that results in localized enhancement of the excitation field. This secondary field induces Raman dipoles in the sample that radiate to the far-field. Because in this process the electric field interacts with the tip (**T**), followed by the sample, this process is referred to as the **ST** term. Alternatively, the excitation field can induce Raman dipoles in the sample that then interact with the tip by inducing surface plasmon oscillations at the frequency of the scattered light that reradiate into the far-field, which is known as the **TS** term. The **ST** and **TS** terms are interference terms between the far-field and near-field components. Finally, the excitation field can interact with the tip, followed by the sample, and finally with the tip again (**TST**), which is the conventional TERS signal. The terms in the expansion that need to be considered depend on the experimental setup and the sample, as well as the enhancement factor. For tips with significant enhancement, the **TST** term dominates, and the other terms can be ignored, which is the case for samples where **S** is small, as is generally true for 0D and 1D

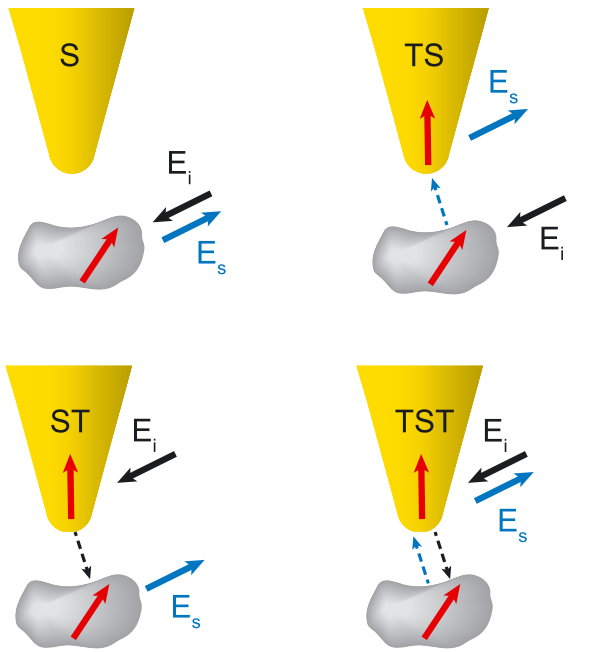

Figure 1. Sketches of the interaction series in tip-enhanced Raman spectroscopy. The black and blue arrows represent electric fields at the excitation (ω_i) and scattered frequency (ω_s), respectively. The red arrows represent the induced dipoles in the sample or the tip. The dashed black and blue arrows indicate interactions between the tip and sample.

materials. However, for spatially extended samples, such as graphene and other 2D materials, both the **ST** and **TS** terms need to be considered. For a strongly focused radial beam, the out-of-plane *z*-component is significantly stronger than the in-plane components. Therefore, the excitation field interacts strongly with the tip, and the **ST** term dominates over the **TS** term. Therefore, the TERS process in graphene often can be represented by only considering the **ST** and **TST** terms for a strongly focused radial excitation (Fig. 3(a)). For 2D materials, the **S** term can be significant, but it has no dependence on the tip-sample separation and therefore is a DC offset for the TERS signal. The case is similar for side illumination of the tip using a linear polarized excitation (Fig. 3(c)). The section on Coherence Effects provides the mathematical foundation for these calculations and the full derivation can be found in Cançado *et al*.[47]

The additional scattering terms have important consequences for understanding the enhancement of the TERS process. Because the conventional TERS signal results from the **TST** term, the total enhancement factor in this case is determined by the enhancement of the excitation and emission fields, $f(\omega_i)^2 f(\omega_s)^2 \approx f(\omega_i)^4$, where f is the field enhancement factor and ω_i and ω_s are the optical frequencies of the excitation and scattered fields, respectively. However, this equation is not valid once the additional scattering terms are included for samples such as graphene. Therefore, the TERS enhancement in graphene requires more detailed calculations. The theoretical framework is discussed in the Coherence Effects section and in detail in Cançado *et al*.[47] In addition, these scattering terms can complicate the interpretation of the measurements. As an example, for 2D materials, **S** term can reflect off the tip, which causes an increased signal without any near-field contribution. However, the presence of the near-field signal can be verified by acquiring images that show sub-diffraction resolution or by measuring the dependence of the TERS signal on the tip-sample separation.

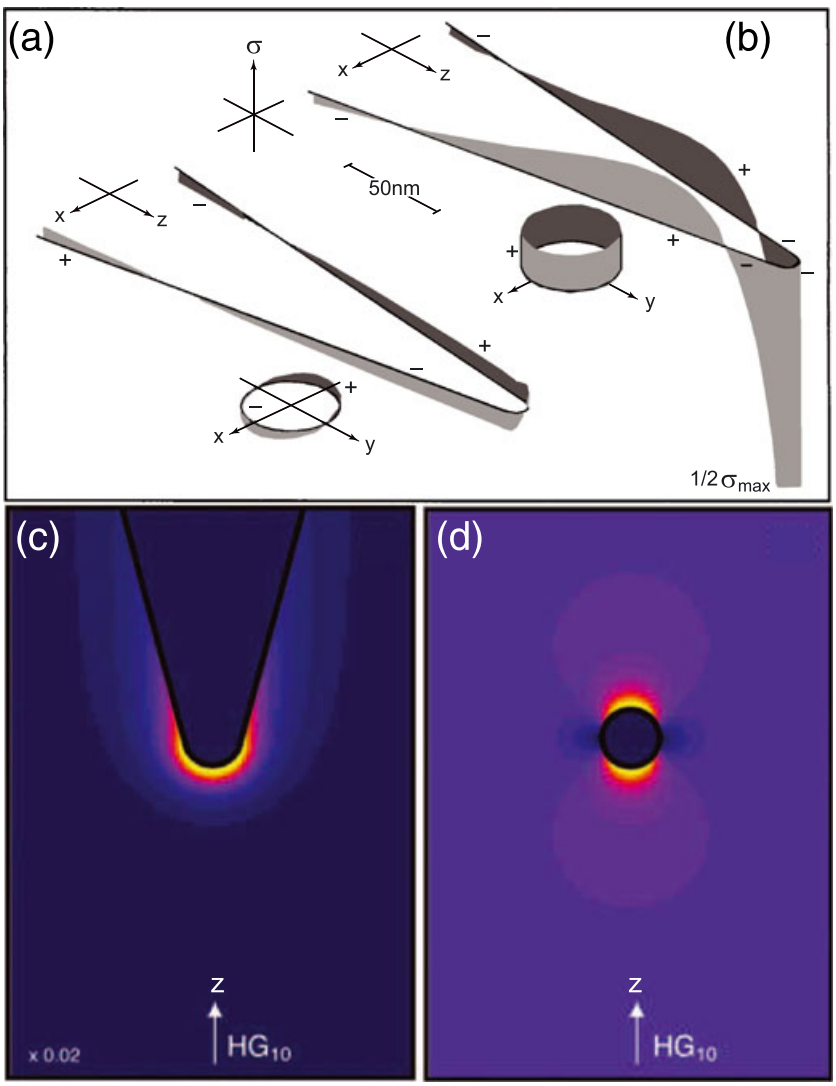

Figure 2. Induced surface charge density on a metal tip. (a) Excitation electric field is polarized along the *x*-axis perpendicular to the tip shaft, and there is a node in the surface charge at the tip apex. (b) Excitation electric field is polarized parallel to the tip shaft (*z*-axis), which leads to a large charge density at the apex. Adapted from Novotny *et al*.[48] with permission. (c),(d) Calculated field distribution with the excitation field polarized along the *z*-axis (HG_{10} mode) for a metal tip and a spherical metal particle, respectively, which results in a significant field enhancement. The spherical metal particle qualitatively agrees with the metal tip, indicating that metal tips can be treated as spherical particles. Adapted from Novotny and Hecht[50] with permission.

To maximize the field enhancement, the polarization of the excitation field must be considered. When the excitation field is polarized perpendicular to the metal tip shaft (Fig. 2(a)), the plasmon is delocalized along the tip and leads to a modest field enhancement. However, when the excitation field is polarized parallel to the tip shaft, the surface charge density at the tip apex is significantly larger because of the geometrical confinement and leads to a large field enhancement, as shown in Fig. 2(b). This effect is commonly referred to as the lightning rod effect, where the tip apex behaves as a singularity and results in large secondary fields. The enhancement of the tip is determined by several factors, including the geometrical shape and the material, which determine the plasmon resonance of the tip. While the discussion thus far has emphasized extended metal tips, these are more difficult to treat theoretically. Figure 2 (c),(d) shows the calculated field distribution for an extended metal tip and a metal sphere excited with an electric field polarized along the *z*-axis.[49,50] It is important to note that the two field distributions qualitatively agree, which means spherical particles can be used as an approximation for extended tips in calculations.

Experimental setup

The TERS microscopy combines Raman and scanning probe microscopy, such as atomic force microscopy (AFM) or scanning tunneling microscopy, which allows for a constant tip-sample distance of a few nanometers to be maintained. The same microscope objective is used for excitation and collection, and the resulting signal is sent to either a spectrometer and charge-coupled device or a single photon counting module in conjunction with a narrow bandpass filter (full-width-at-half-maximum $<$ 10 nm) to select out the Raman mode of interest. The tip is positioned in the focus, and the sample is raster-scanned through the focus to build up images.

As illustrated in Fig. 2, the tip needs to be excited using an electric field polarized along the tip shaft. There are three general experimental approaches, which are illustrated in Fig. 3. The first method utilizes a high NA microscope objective for excitation and collection. This allows for the signal from the entire lower half space to be collected. In order to efficiently excite the tip, the incident electric field has to be oriented along the tip axis (z-direction). This can be accomplished by strongly focusing a radially polarized beam using a high NA objective, which leads to a strong z-field. It is important to note that a high NA objective is required to create the z-fields because they arise from polarization mixing in non-paraxial beams. Figure 3(b) shows the strength of the z-lobe as a function of NA for an oil immersion objective (n = 1.518) for linearly (black) and radially (red) polarized beams for the transmission geometry (Fig. 3(a)). This experimental approach is the primary focus of this review. In the second experimental approach (Fig. 3(c)), the tip is illuminated from the side using linearly polarized light aligned along the tip axis. In this case, a high NA objective is not required to generate electric fields polarized along the tip axis. This approach has the advantage of allowing for measurements on nontransparent samples, such as silicon, as well as a simpler optical setup. However, because the illumination and collection are from the side, the collection angle is limited, and a large area on the sample is illuminated, which increases the far-field background and limits the collection efficiency. The third approach is top illumination with the tip at an angle. Similar to side illumination, this allows for the use of nontransparent substrates with the additional benefit of a simpler optical design and the potential to use higher numerical aperture objectives that increase the excitation and collection efficiency. The properties of the tip determine the resolution and enhancement of the TERS signal, and it requires fabrication to maximize the performance. Two examples of TERS tips are shown in Fig. 3(e): an electro-chemically etched gold tip (left)[51] and a template striped silver tip (right).[52] For experimental applications of TERS on 2D materials, the excitation polarization and tip geometry shown in Fig. 3 are not ideal for coupling to the in-plane Raman modes of the material. However, this can be improved by reengineering the tip geometry. Despite this limitation, the results presented demonstrate that TERS is capable of resolving nanoscale features in graphene samples.

Figure 3(f) shows a TERS image of the G′ band of a single layer graphene crystal. As a comparison, a confocal image of the same region with the color contrast scaled by $\times$3 is shown in the inset.[53] These images illustrate both the resolution improvement and signal enhancement of TERS. The signal enhancement as well as the spectral information from TERS is further illustrated by the Raman spectra with (red) and without (black) the tip presented in Fig. 3(g), which were acquired in the center (black square in Fig. 3(f)) and at the edge (black circle in Fig. 3(f)) in the top and bottom panels, respectively.[53] These spectra show the two primary bands in graphene, the G and G′ bands, as well as the D band localized at the edge of crystal. Figure 3(f),(g) demonstrates the capability of TERS to image and characterize graphene at the nanoscale.

Coherence effects

In conventional Raman scattering, the scattering process is generally treated as a spatially incoherent process, which means that spatially distinct locations on the sample are uncorrelated. Therefore, the signal from each location can be summed, and the total scattered signal, S, is proportional to the volume of the scatterer, V. This leads to the expression,

$$S \propto V|\epsilon \cdot \overleftrightarrow{\alpha}\, E|^2 \tag{2}$$

where ϵ is a unit vector defining the scattering polarization direction and α is the polarizability tensor of the volume element.[23,24] This approach has been justified from coherence theory because spatial correlations from an incoherent source smaller than $\lambda/2$ do not propagate into the far-field.[54] Therefore, Raman scattering at the macroscopic scale is spatially incoherent, because the spatial correlation length, L_c, is typically an order of magnitude shorter than the wavelength of light. However, this approach is not valid once the near-field components of the light-matter interactions are included for scattering processes at the nanoscale.[55–60] In this regime, the near-field signal contains information about the nanoscale sample correlations that are unobservable in the far-field. As a result of coherence effects in the near-field, Raman signal depends on the mode symmetry, the spatial confinement, and L_c. Therefore, TERS allows for optical characterization of nanoscale spatial correlations, which govern many relevant properties for the progression of nanoscale devices. Raman coherence effects in the near-field were investigated theoretically in a number of studies[47,51,61] and experimentally in other studies.[51,53]

As discussed previously, in the near-field regime, Eqn (2) is no longer valid, and nanoscale correlations need to be included in the theoretical formalism. Figure 4 illustrates two individual

Journal of RAMAN SPECTROSCOPY

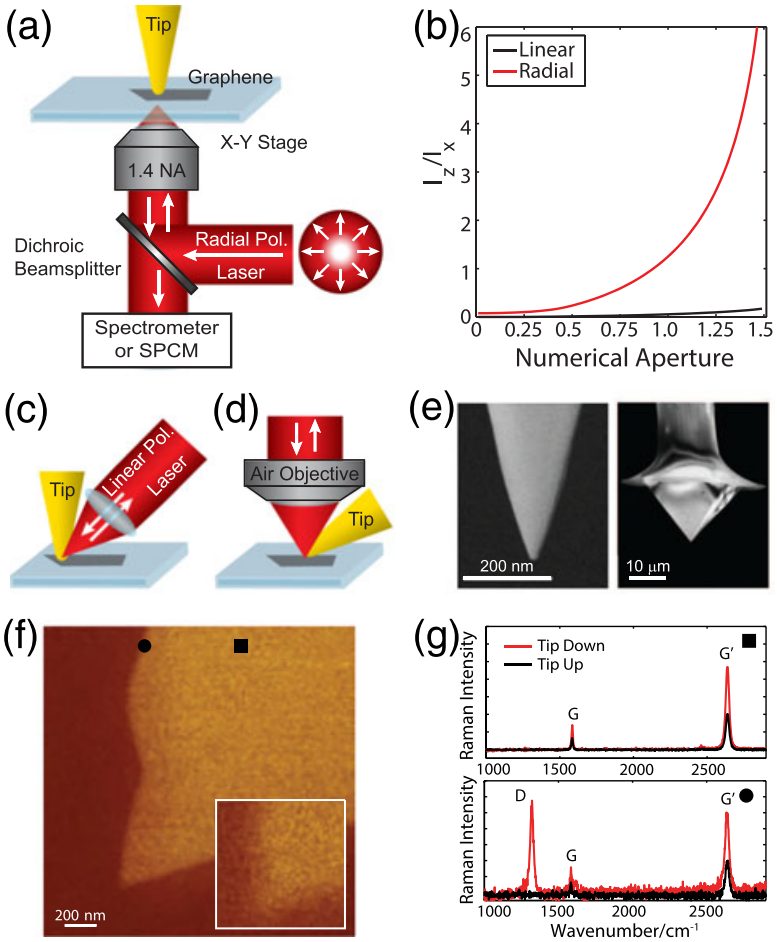

Figure 3. (a) Experimental tip-enhanced Raman spectroscopy (TERS) setup for transparent samples using a high NA objective and a radially polarized beam. (b) Plot of the electric field in the z-direction as a function of NA in oil ($n = 1.518$) for linearly (black) and radially (red) polarized beams. (c) Side and (d) top illumination TERS setups. (e) Scanning electron microscopy images of TERS tips. Left: etched gold tip. Adapted from Cançado *et al.*[51] with permission. Right: pyramid tip. Adapted from Beams *et al.*[52] with permission. (f) TERS image of the G′ band in single layer graphene. Inset: confocal image of the same area with the color contrast scaled by ×3. (g) Raman spectra of graphene acquired in the center (top panel) and at the edge (bottom panel) of a flake with (red) and without (black) the tip. The locations are indicated by the black square and circle in (f), respectively. Adapted from Beams *et al.*[53] with permission.

scattering events at locations $\mathbf{r}_1$ and $\mathbf{r}_2$ in the scattering domain D that is illuminated by an incident field $\mathbf{E}(\omega)$. For scatterer separations $|\mathbf{r}_1 - \mathbf{r}_2|$ significantly larger than L_c, the scattered fields add incoherently at the detector as expected for far-field Raman scattering. However, on length scales smaller than L_c, the scattered fields add coherently at the detector. In conventional far-field measurements, a large sample volume is probed, and therefore, the sample correlations on small length scales are averaged out. However, in the near-field, the interaction volume is localized, and nanoscale sample correlations manifest as interference in the scattered signal.

Mathematically, this can be understood by considering a medium irradiated by a monochromatic field, $\mathbf{E}(\omega)$, which leads to a scattered field, $\mathbf{E}^s$ at frequency ω_s, at the detector location, $\mathbf{r_0}$, which can be expressed as

$$\mathbf{E}^s(\mathbf{r_0};\omega_s) = \frac{\omega_s^2}{\epsilon_0^2 c^2}\int_D d\mathbf{r}^3 \overleftrightarrow{G}(\mathbf{r_0},\mathbf{r};\omega_s)\mathbf{p}^\gamma(\mathbf{r}) \qquad (3)$$

where ϵ_0 and c are the free-space permittivity and speed of light, respectively. $\mathbf{p}^\gamma(\mathbf{r})$ is the induced Raman dipole associated with

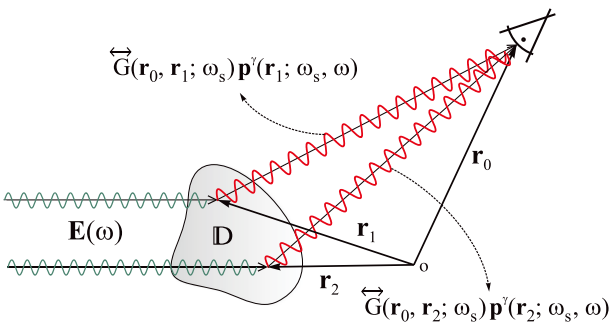

Figure 4. Illustration of two individual scattering paths associated with a scatterer domain D irradiated by the field **E**. On length scales $|\mathbf{r}_1 - \mathbf{r}_2|$ smaller than the phonon correlation length L_c of a vibrational mode γ, the partial fields generated by the Raman dipoles $\mathbf{p}^\gamma(\mathbf{r}_1)$ and $\mathbf{p}^\gamma(\mathbf{r}_2)$ add coherently at location $\mathbf{r_0}$ of the detector. For length scales larger than L_c, there is no phase correlation between the scattering events; hence, the partial fields at the detector add incoherently. Adapted from Cançado *et al.*[47] with permission.

the vibrational mode, γ, at position $\mathbf{r}$ in the scattering domain D, and $\overleftrightarrow{G}(\mathbf{r_0}, \mathbf{r})$ is the outgoing Green's function. By using the Raman polarizability tensor, $\overleftrightarrow{\alpha}^{\gamma}$, the induced Raman dipole can be expressed as $\mathbf{p}^{\gamma}(\mathbf{r}) = \overleftrightarrow{\alpha}^{\gamma}\mathbf{E}$.

The signal $\mathbf{S}(\mathbf{r_0})$ at the detector is proportional to the ensemble time average of the scattered fields. Using Eqn (3), $\mathbf{S}(\mathbf{r_0})$ is calculated by

$$\begin{aligned}\mathbf{S}(\mathbf{r_0}) &= \left\langle \mathbf{E}^{s*}(\mathbf{r_0}) \cdot \mathbf{E}^{s}(\mathbf{r_0}) \right\rangle \\ &= \frac{\omega_s^4}{\epsilon_0^2 c^4} \int_D d\mathbf{r}_1^3 \int_D d\mathbf{r}_2^3 \left\langle \overleftrightarrow{G}^{*}(\mathbf{r}_0, \mathbf{r}_1)\mathbf{p}^{\gamma *}(\mathbf{r}_1) \cdot \overleftrightarrow{G}(\mathbf{r}_0, \mathbf{r}_2)\mathbf{p}^{\gamma}(\mathbf{r}_2) \right\rangle \\ &= \frac{\omega_s^4}{\epsilon_0^2 c^4} \int_D d\mathbf{r}_1^3 \int_D d\mathbf{r}_2^3 \left\langle \overleftrightarrow{\alpha}^{\gamma *}(\mathbf{r}_1)\overleftrightarrow{\alpha}^{\gamma}(\mathbf{r}_2) \right\rangle \overleftrightarrow{G}^{*}(\mathbf{r}_0, \mathbf{r}_1)\mathbf{E}^{*}(\mathbf{r}_1) \\ &\quad \cdot \overleftrightarrow{G}(\mathbf{r}_0, \mathbf{r}_2)\mathbf{E}(\mathbf{r}_2)\end{aligned} \tag{4}$$

where $\left\langle \overleftrightarrow{\alpha}^{\gamma *}(\mathbf{r}_1)\overleftrightarrow{\alpha}^{\gamma}(\mathbf{r}_2) \right\rangle$ accounts for the correlation between scattering dipoles at locations $\mathbf{r}_1$ and $\mathbf{r}_2$. As discussed previously, the Raman process is generally treated as spatially incoherent, which means the correlation length can be replaced by a Dirac delta function $\delta(\mathbf{r}_1 - \mathbf{r}_2)$. In this case, the integral in Eqn (4) is over the scattering volume and leads to Eqn (2). However, as the length scale of the light-matter interactions approaches the correlation length, as is the case for TERS, this is no longer valid, and the correlation function needs to be considered.

The sample correlations can be accounted for by using a Gaussian correlation function as an ansatz of the form

$$\left\langle \overleftrightarrow{\alpha}^{\gamma *}(\mathbf{r}_1)\overleftrightarrow{\alpha}^{\gamma}(\mathbf{r}_2) \right\rangle = \tilde{\alpha}^{\gamma}(\mathbf{r}_1)\tilde{\alpha}^{\gamma}(\mathbf{r}_2)\, \frac{e^{-(|r_1 - r_2|^2/L_c^2)}}{\pi L_c^2} \tag{5}$$

The incoherent case is represented by the limit that $L_c \to 0$, which results in the term $e^{-(|r_1 - r_2|^2/L_c^2)}/\pi L_c^2$ reducing to a delta function; for a fully coherent process ($L_c \to \infty$) that term is a constant. For coherent processes, the scattered fields from spatially distinct points within the correlation length can constructively or destructively interfere depending on the relative phase between the points, which is determined by the symmetry of the Raman mode being considered. The degree to which the fields within an interaction volume interfere is represented by the correlation function in Eqn (5). This means that the relative intensities of the Raman modes in the near-field can be significantly different than in the far-field. Beyond the impact of the mode symmetries, the dimensionality is also significant because it determines the number of lattice points that are added coherently in the process. In a related theoretical paper, the coherence properties of thermal phonons were investigated.[62]

Graphene represents an excellent material to study spatial correlations using TERS because the three main Raman modes have different mode symmetries and dimensionalities. As discussed in the introduction, the G and G′ bands have different symmetry, belonging to the E_{2g} and A_1 irreducible representation, respectively. In addition, the D band originates from defects and edges, which is 0D for point defects and 1D for edges. Therefore, the near-field Raman signal of graphene allows for the phonon correlations and spatial coherence of the Raman process to be studied in these varied cases.

In the near-field regime, the coherence effects for the G and G′ bands are opposite, showing destructive and constructive interference, respectively. Figure 5(a),(b) illustrates this difference for the **TST** term. As discussed earlier, the excitation field creates a vertical dipole along the tip axis, which in turn induces Raman dipoles in the sample. Depending on the relative phase between the locations on the sample, as determined by the Raman matrices, the local fields add constructively or destructively. The induced Raman dipoles for the G band have opposite phases, whereas they have the same phase for the G′ band. For example, for the E_{2g1} mode, the in-plane induced Raman dipoles in the x-direction are in phase with the excitation field, whereas the in-plane induced Raman dipoles in the y-direction are out of phase with the excitation field. For A_1 modes, all the induced Raman dipoles are in phase with the excitation field.[47,53] The Raman scattering signal then excites a dipole at the tip at the frequency of the scattered light before scattering to the detector. Because of the phase differences in the two bands, the Raman fields add destructively and constructively for the G and G′ bands at the tip, respectively. Because the interference effects are in the near-field and occur at the tip, they are only present in the **TST** term. Therefore, to measure the interference effects requires significant field enhancement to ensure the **TST** term dominates. Furthermore, the sharpness of the tip is important because the interaction area must be of similar spatial extent to L_c. Finally, the measured interference effects are also dependent on the experimental geometry.

The near-field coherence effects were calculated in previous studies,[47,51,61] for carbon nanotubes and graphene using the formalism outlined in Eqn (4), and the rigorous details of the theory are presented in Cançado *et al*.[47] The near-field interference effects can be investigated by measuring the Raman signal as a function of the separation distance between the tip and the sample, z_{ts}, because the signal transition from a conventional incoherent Raman signal in the far-field regime ($z_{ts} \to \infty$) into the near-field regime ($z_{ts} \to r_{tip}$, where r_{tip} is the tip radius) is dominated by coherence effects. Note that z_{ts} is defined as the distance of the effective tip dipole from the surface, which means the minimum tip-sample separation is r_{tip}. Figure 5(c),(d) shows the calculated tip-sample curves for $L_c = 0$ nm and $L_c = 50$ nm at a graphene edge. For the spatially uncorrelated case ($L_c = 0$ nm), the G and G′ approach curves coincide. Despite the D band having the same symmetry as the G′ band, the D band signal has a steeper distance dependence because the origin is lower dimensional (edge *vs* interior). As L_c increases, the steepness of the distance dependence decreases for all the bands, and the interference effects manifest in the signals for the G and G′ bands, as seen by the striking difference in Fig. 5(d).[53] These curves indicate that L_c can be determined by measuring the z_{ts} dependence of the Raman signal. Figure 5(e) shows an experimentally acquired approach curve at a graphene edge. Fitting the data with the theoretical curves (solid lines) gives $L_c = 30$ nm for the three bands.[53] The measured phonon correlation length using TERS is in excellent agreement with the value extracted from nano-graphite samples.[63] Because L_c is a fitting parameter in the theoretical treatment, this approach is suitable for a wide range of samples including characterizing the influence of defects, substrates, and stacking on L_c. Furthermore, this treatment can directly be extended to other 2D materials.

Journal of RAMAN SPECTROSCOPY

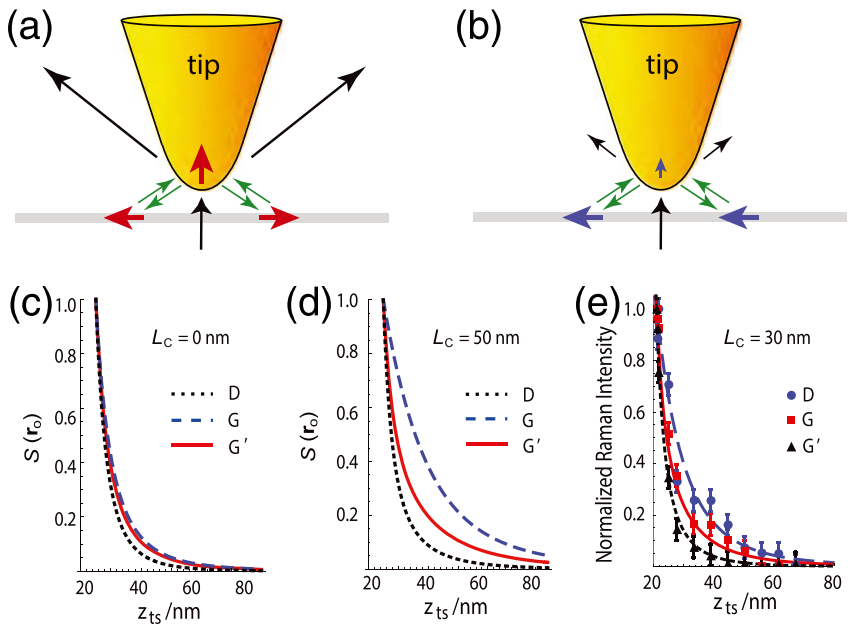

Figure 5. (a),(b) Sketches of the tip-enhanced Raman spectroscopy process. The incident field induces a vertical dipole in the tip that interacts with the sample (green arrows), which in turn acts back on the tip at the frequency of the scattered light (green arrows) before the fields are scattered out to the detector. The strength of the scattered signal depends on the relative phase of the induced dipoles in the sample (horizontal red and blue arrows). The emission dipoles on the sample add constructively for the G′ band and destructively for the G band, as shown in (a),(b), respectively. Adapted from Beams *et al.*[53] with permission. (c),(d) Theoretical dependence of the signal on the tip-sample separation (z_{ts}) for the D, G, and G′ bands. The curves are calculated with two different phonon correlation lengths: $L_c = 0$ nm and $L_c = 50$ nm. The signal $S(\mathbf{r_0})$ is normalized to 1 for $z_{ts} = 25$ nm, which corresponds to the closest tip-sample distance. (e) Experimental dependence of the signal on z_{ts} at a graphene edge. Adapted from Beams *et al.*[53] with permission.

TERS characterization of edges and defects

One of the most prominent applications for TERS for graphene is characterizing local defects. Generally, defects affect material properties, and therefore, identification and characterization of defects is crucial for optimizing device performance. Additionally, material properties are often controlled using substitutional doping, which can also act as defects in the material. Raman spectroscopy is particularly important for characterizing defects in graphene due to the disorder-induced D band, which is a defect allowed Raman mode. The D band has the same symmetry as the G′ band, but instead of two phonons being involved in the scattering process, a defect fulfills the momentum conservation to make the process Raman active. In this section, two types of defects will be reviewed: edges and point defects. Conventional Raman spectroscopy has been used to explore these two types of defects in great detail, which has allowed for the defect density, edge chirality, and defect type to be quantitatively determined.

Edges

Graphene edges can be viewed as a unique type of defect, because the edge breaks the translational symmetry of the graphene lattice. To fulfill the momentum conservation requirement for the Raman process, the edges also have to have armchair chirality with the excitation polarization aligned with the edge. In contrast, the momentum vector for zig-zag edges is in the wrong direction to conserve momentum.[16] Therefore, Raman spectroscopy provides a powerful method to characterize graphene edges and has been extensively used.[16–18,64–67] For this process to be Raman active, the excited electrons have to scatter off the edge. The length scale over which the process is Raman active is determined by the coherence length of the electrons involved in the scattering process. By utilizing prior information about the sample, this length scale has been measured using conventional Raman spectroscopy to be $\approx$ 5 nm,[18] which is in excellent agreement with the estimates using the lifetime of the photo-excited electron.[17] While these approaches have measured or estimated fundamental material properties, they are still diffraction limited and are unable to spatially map edges at the nanoscale. However, TERS is well suited to measure the D band at edges as has been demonstrated.[28,30,31,33,38,53,68] Figure 6(a) shows the topographic image of a graphene crystal. The corresponding TERS image with the D (green), G (blue), and G′ (red) bands overlaid is shown in Fig. 6(b). These images of graphene edges show that the D band is highly localized[31,38,53,68] as expected from the far-field Raman measurements. In addition to the localized D band at the edge, there is also an intrinsic line defect that is visible in the TERS image. Spectra acquired with (black) and without the tip (red) at the labeled locations are shown in Fig. 6(c) and demonstrate the ability of TERS to enhance weak D band signals from localized defects. Detailed characterization of the TERS hyperspectral linescans for the intensities of the G and D bands (Fig. 6(d),(e), respectively) showed that the D band localization at an edge is $\approx$ 4 nm,[31] which is in excellent agreement with the far-field measurements.[18] These results also demonstrate that TERS measurements are suitable to characterize grain boundaries or edges in stacked heterostructures.

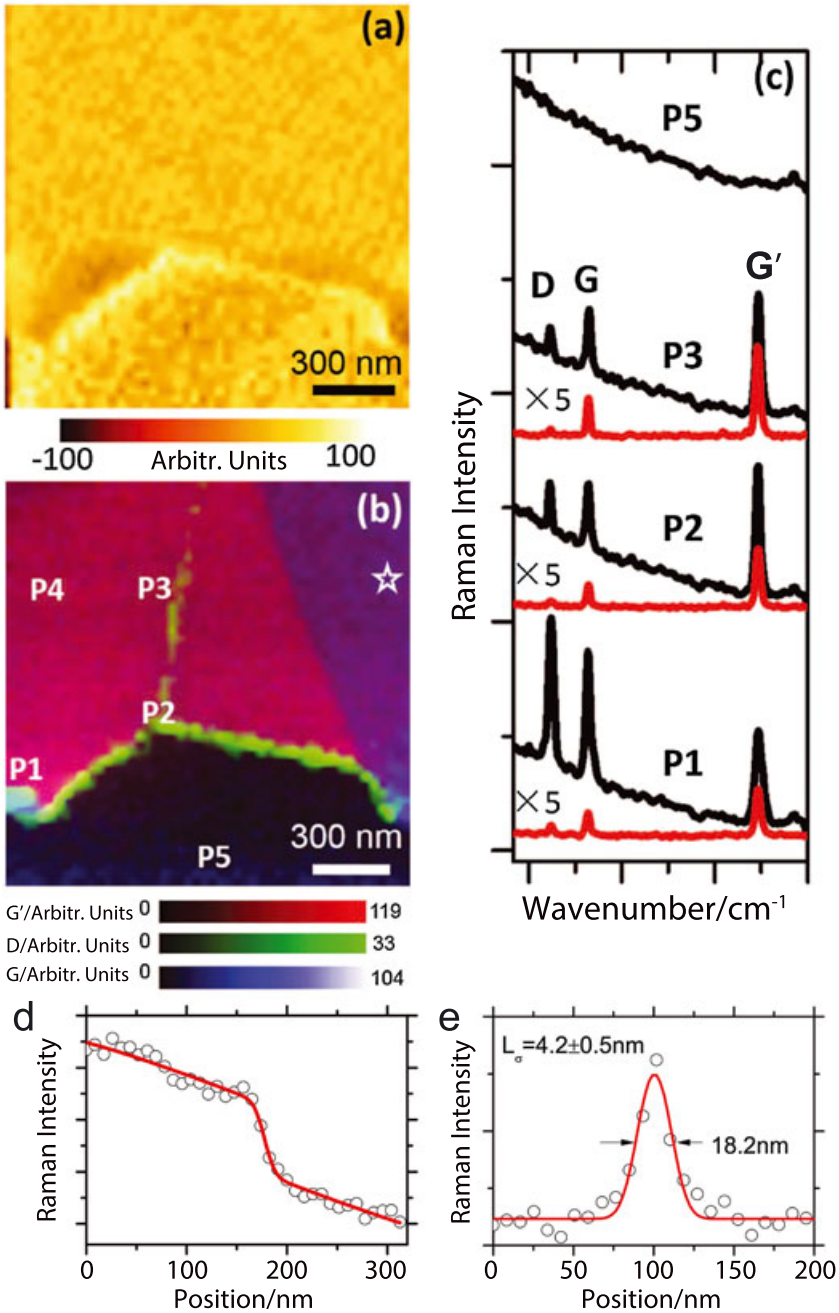

Figure 6. (a) Topographic image of a graphene crystal. (b) Tip-enhanced Raman spectroscopy image of the graphene crystal with the D (green), G (blue), and G′ (red) overlaid. (c) Spectra with (black) and without (red) the tip at the locations labeled in (b). Adapted from Su *et al.*[34] with permission. (d),(e) Hyperspectral linescans of the G and D bands intensities, respectively. The D band localization, L_σ, was measured to be $L_\sigma = 4.2 \pm 0.5$ nm. Adapted from Su and Roy.[31] with permission.

Localized defects

Device performance is often limited by defects in the material. Point defects have been extensively characterized using conventional Raman spectroscopy including the spatial extent of the Raman active area[1] and quantifying the defect density from the ratio of the D and G band intensities.[1,2,69] Similar to edges, the spatial extent of the D band around a point defect is $\approx$ 5 nm. However, because a point defect has a radius of a few nanometers, the D band signal from a single point defect is insufficient to measure using conventional Raman spectroscopy. Therefore, TERS provides both the resolution and signal enhancement required to study single point defects.

Single point defects created in graphene by ion bombardment were characterized using TERS in Mignuzzi *et al.*[32] The topographic image of a graphene crystal is shown in Fig. 7(a). By using TERS, highly localized point defects were imaged as shown in Fig. 7(b). Because the signal from single point defects is very low, the signal enhancement from TERS is necessary to image single point defects. This is illustrated in Fig. 7(c), which shows spectra with the tip on a defect (red), off a defect (blue), and without the tip present (black).[32] In this case, the signal increase for the D

Journal of RAMAN SPECTROSCOPY

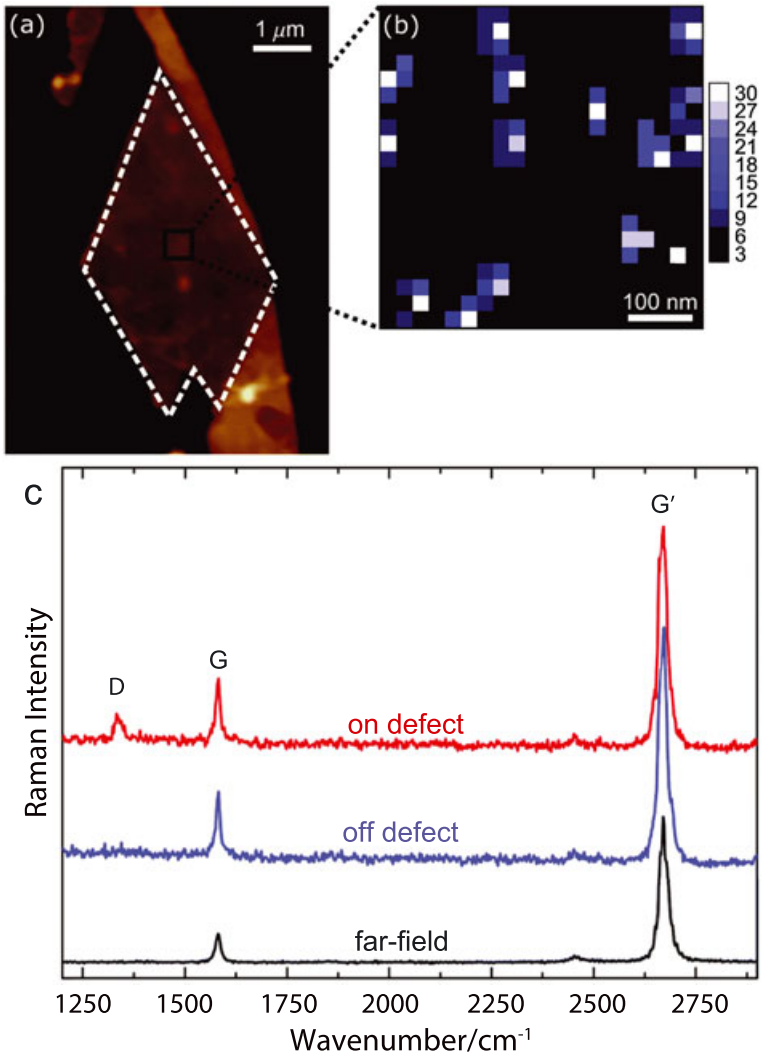

Figure 7. (a) Topography of a graphene crystal. (b) D band image of point defects. (c) Tip-enhanced Raman spectroscopy spectra acquired on (red) and off (blue) a defect with the far-field image in black. Adapted from Mignuzzi *et al*.[32] with permission.

band due to the presence of the tip is much larger than for the other bands, because the D band is originating from point defects with minimal confocal Raman signal. In contrast, the G and G′ bands are active over the entire sample, which leads to an appreciable confocal Raman signal and a more modest signal increase. These measurements demonstrate that TERS is well suited to characterize single defects in graphene, which are not observed in conventional Raman spectroscopy. Similarly, the intrinsic defects from growing graphene on copper as well as surfaces adsorbates were studied in Stadler *et al*.[29]

These studies demonstrate the ability of TERS to identify nanoscale defects, which could not be imaged using conventional Raman spectroscopy. Furthermore, TERS has the ability to measure the local properties of different defect types, which would strengthen the conventional Raman studies of defects. By combining the detailed understanding of the Raman signatures of different types of defects, such as point-defects, grain-boundaries, and edges, with the spatial resolution and sensitivity of TERS can facilitate quantitative defect characterization at the nanoscale.[1,2,70]

Strain

An additional application for TERS is to characterize the strain in graphene. The performance of graphene devices often depends on the mechanical strain, which includes device performance degradation from unintended strain as well as a method to controllably modify the material properties. Material strain, including graphene, is frequently characterized using Raman spectroscopy. The two most commonly studied types of strain are uniaxial and biaxial. Under compressive (tensile) strain, the G and G′ bands blueshift (redshift). In the case of uniaxial strain, the G band splits into two peaks, and the G′ band widens or splits,[3–5,8] whereas for biaxial strain, the widths are unaffected.[6,7] However, the resolution of conventional Raman spectroscopy is insufficient to characterize nanoscale strain. While AFM-based force-displacement techniques have been extensively used to study the mechanical properties with localized loads,[71] this approach requires suspended samples and therefore cannot characterize the static strain intrinsic to samples or as a result of fabrication. There has been work combining scanning force-displacement measurements with conventional Raman scattering, which validates the complimentary aspects of these two characterization

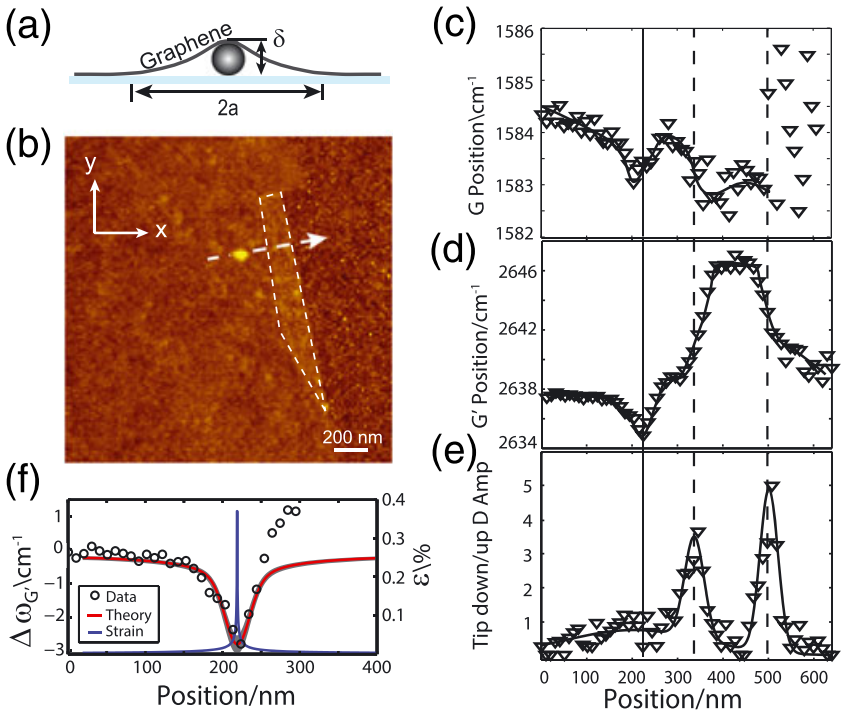

Figure 8. (a) Sketch of a spherical particle displacing the graphene by δ over a range of 2*a*. (b) Atomic force microscopy image of the graphene sample and the particle. The white arrow indicates the location, taken tail to head, of the hyperspectral linescan shown in (c)–(e). (c),(d) Center wavenumber for the G and G′ bands, respectively. (e) D band amplitude ratio with and without the tip. Black lines are guides for the eye. (f) Plot of the Raman shift of the G′ band, $\Delta\omega_{G'}$ (circles) from (c). The fit is shown in red, and the total strain profile, ϵ, is shown in blue. A strain of $\epsilon = 0.37$ % was used for fitting the Raman data. Adapted from Beams *et al.*[38] with permission.

methods.[72] Nanoscale strain in graphene has also been investigated theoretically.[73] TERS on graphene allows for the intrinsic strain to be characterized with resolution at the nanoscale, which has the potential to provide powerful insights into local properties of devices.

The ability of TERS to characterize local intrinsic strains was demonstrated in Beams *et al.*[38] using the transmission-based TERS setup described in Experimental Setup section. As shown in Fig. 8(a), a 5 nm particle underneath the graphene exerted a local radial strain on the graphene. Because the small particle applies a local force on the flake, this type of strain is analogous to force-displacement measurements where the AFM tip has been replaced by the particle. Therefore, the Raman measurements can be compared with force-displacement results. Because of the size of the particle, the strain was unobservable using conventional Raman spectroscopy, which provides an excellent demonstration that TERS can measure nanoscale strain in graphene.

The topographic image of the graphene, particle, and folded region is shown in Fig. 8(b). To characterize the strain, a hyperspectral line scan was acquired tail to head along the white arrow, and the position of the G and G′ bands is shown in Fig. 8(c),(d). Both bands redshift (solid black vertical line) as a result of the strain, as expected for radial tensile strain. The folded region in Fig. 8(b) (white dashed lines), which is topographically thicker, is also clearly seen in the position of the bands between the dashed vertical lines in Fig. 8(c)–(e). The ratio of D band amplitudes with and without the tip is shown in Fig. 8(e), and a strong D band is seen localized at the edges of the folded region as expected. Fitting the shift in the G′ position, $\Delta\omega$, shows that $\Delta\omega \propto \epsilon_r \propto r^{-2/3}$, where ϵ_r is the radial strain along the radial direction r in-plane from the particle. As discussed previously, these results illustrate that TERS can be used to characterize intrinsic strain in material at the nanoscale, which is of great importance for device applications.

Outlook

TERS is a powerful technique for characterizing graphene properties at the nanoscale. As discussed, it has provided important insights into the localization of defects[29,32,34] and edges[31] as well as imaging of contaminants[29] and mechanical strain[38] with nanometer resolution. These results focusing primarily on illustrating the capabilities of TERS to study graphene demonstrate that TERS is capable of characterizing the chemical and structural properties of graphene at a resolution that is relevant for nanotechnology. Furthermore, with the growing emphasis on Van der Waals heterostructures with graphene, boron nitride, and transition metal dichalcogenides, it is increasingly important to implement techniques capable of studying the boundaries and interfaces of these stacked structures.

As discussed in section on Coherence Effects, TERS also provides optical access to the spatial phonon correlations that are inaccessible in conventional Raman scattering.[47,51,53,61] This opens new possibilities for TERS to study fundamental material properties that cannot be accessed using other optical techniques, such as the impact of dopants, strain, defects, and processing on the phonon correlations. Coupled with transport measurements, this provides a detailed understanding of the material that will aid device applications. While this was only demonstrated for graphene, it can be applied to other low dimensional materials including transition metal dichalcogenides, nanotubes, and more complex hybrid materials.

Acknowledgements

The author would like to thank L. G. Cançado, S. J. Stranick, and G. W. Bryant for valuable discussions and critical reviews of the manuscript.

References

[1] M. M. Lucchese, F. Stavale, E. H. Martins Ferreira, C. Vilani, M. V. O. Moutinho, R. B. Capaz, C. A. Achete, A. Jorio, *Carbon* **2010**, *48*, 1592.
[2] L. G. Cançado, A. Jorio, E. H. Martins Ferreira, F. Stavale, C. A. Achete, R. B. Capaz, M. V. O. Moutinho, A. Lombardo, T. S. Kulmala, A. C. Ferrari, *Nano Lett.* **2011**, *11*, 3190.
[3] T. M. G. Mohiuddin, A. Lombardo, R. R. Nair, A. Bonetti, G. Savini, R. Jalil, N. Bonini, D. M. Basko, C. Galiotis, N. Marzari, K. S. Novoselov, A. C. Ferrari, *Phys. Rev. B* **2009**, *79*, 205433.
[4] M. Huang, H. Yan, T. F. Heinz, J. Hone, *Nano Lett.* **2010**, *10*, 4074.
[5] O. Frank, M. Mohr, J. Maultzsch, C. Thomsen, I. Riaz, R. Jalil, K. S. Novoselov, G. Tsoukleri, J. Parthenios, K. Papagelis, L. Kavan, C. Galiotis, *ACS Nano* **2011**, *5*, 2231.
[6] F. Ding, H. Ji, Y. Chen, A. Herklotz, K. Dörr, Y. Mei, A. Rastelli, O. G. Schmidt, *Nano Lett.* **2010**, *10*, 3453.
[7] J. Zabel, R. R. Nair, A. Ott, T. Georgiou, A. K. Geim, K. S. Novoselov, C. Casiraghi, *Nano Lett.* **2012**, *12*, 617.
[8] H. Shioya, M. F. Craciun, S. Russo, M. Yamamoto, S. Tarucha, *Nano Lett.* **2014**, *14*, 1158.
[9] A. Das, S. Pisana, B. Chakraborty, S. Piscanec, S. K. Saha, U. V. Waghmare, K. S. Novoselov, H. R. Krishnamurthy, A. K. Geim, A. C. Ferrari, A. K. Sood, *Nature Nanotech.* **2008**, *3*, 210.
[10] A. Jorio, M. S. Dresselhaus, R. Saito, G. Dresselhaus, *Raman Spectroscopy in Graphene Related Systems* (first edition), Wiley-VCH, Weinheim, Germany, **2011**.
[11] A. C. Ferrari, J. C. Meyer, V. Scardaci, C. Casiraghi, M. Lazzeri, F. Mauri, S. Piscanec, D. Jiang, K. S. Novoselov, S. Roth, A. K. Geim, *Phys. Rev. Lett.* **2006**, *97*, 187401.
[12] Y. Hao, Y. Wang, L. Wang, Z. Ni, Z. Wang, R. Wang, C. K. Koo, Z. Shen, J. T. L. Thong, *Small* **2010**, *6*, 195.
[13] V. Carozo, C. M. Almeida, E. H. Martins Ferreira, L. G. Cançado, C. A. Achete, A. Jorio, *Nano Lett.* **2011**, *11*, 4527.
[14] A. Eckmann, A. Felten, A. Mishchenko, L. Britnell, R. Krupke, K. S. Novoselov, C. Casiraghi, *Nano Lett.* **2012**, *12*, 3925.
[15] L. G. Cançado, M. G. da Silva, E. H. Martins Ferreira, F. Hof, K. Kampioti, K. Huang, A. Pénicaud, C. A. Achete, R. B. Capaz, A. Jorio, *2D Materials* **2017**, *4*, 025039.
[16] L. G. Cançado, M. A. Pimenta, B. R. A. Neves, M. S. S. Dantas, A. Jorio, *Phys. Rev. Lett.* **2004**, *93*, 247401.
[17] C. Casiraghi, A. Hartschuh, H. Qian, S. Piscanec, C. Georgi, A. Fasoli, K. S. Novoselov, D. M. Basko, A. C. Ferrari, *Nano Lett.* **2009**, *9*, 1433.
[18] R. Beams, L. G. Cançado, L. Novotny, *Nano Lett.* **2011**, *11*, 1177.
[19] A. C. Ferrari, *Solid State Comm.* **2007**, *143*, 47.
[20] L. M. Malard, M. A. Pimenta, G. Dresselhaus, M. S. Dresselhaus, *Phys. Rep.* **2009**, *473*, 51.
[21] A. C. Ferrari, D. M. Basko, *Nature Nanotech.* **2013**, *8*, 235.
[22] R. Beams, L. G. Cançado, L. Novotny, *J Phy: Condensed Matter* **2015**, *27*, 083002.
[23] W. Hayes, R. Loudon, *Scattering of Light by Crystals*, Wiley, New York, **1978**.
[24] M. Cardona, Resonance phenomena, in *Light scattering in solids II*, Springer, **1982**, pp. 19–178.
[25] T. L. Vasconcelos, B. S. Archanjo, B. Fragneaud, B. S. Oliveira, J. Riikonen, C. Li, D. S. Ribeiro, C. Rabelo, W. N. Rodrigues, A. Jorio, C. A. Achete, L. G. Cançado, *ACS Nano* **2015**, *9*, 6297.
[26] Y. Saito, P. Verma, K. Masui, Y. Inouye, S. Kawata, *J. Raman Spectrosc.* **2009**, *40*, 1434.
[27] V. Snitka, R. D. Rodrigues, V. Lendraitis, *Microelectronic Eng.* **2011**, *88*, 2759.
[28] M. Ghislandi, G. G. Hoffmann, E. Tkalya, L. Xue, G. D. With, *Appl. Spectrosc. Rev.* **2012**, *47*, 371.
[29] J. Stadler, T. Schmid, R. Zenobi, *ACS Nano* **2010**, *5*, 8442.
[30] R. Rickman, P. Dunstan, *J. Raman Spectrosc.* **2014**, *45*, 15.
[31] W. Su, D. Roy, *J. Vac. Sci. and Technol. B* **2013**, *31*, 041808.
[32] S. Mignuzzi, N. Kumar, B. Brennan, I. S. Gilmore, D. Richards, A. J. Pollard, D. Roy, *Nanoscale* **2015**, *7*, 19413.
[33] F. Pashaee, F. Sharifi, G. Fanchini, F. Lagugné-Labarthet, *Phys. Chem. Chem. Phys.* **2015**, *17*, 21315.
[34] W. Su, N. Kumar, N. Dai, D. Roy, *Chemical Commu.* **2016**, *52*, 8227.
[35] T. Suzuki, T. Itoh, S. Vantasin, S. Minami, Y. Kutsuma, K. Ashida, T. A. Kaneko, Y. Morisawa, T. Miura, Y. Ozaki, *Phys. Chem. Chem. Phys.* **2014**, *16*, 20236.
[36] S. Vantasin, I. Tanabe, Y. Tanaka, T. Itoh, T. Suzuki, Y. Kutsuma, K. Ashida, T. Kaneko, Y. Ozaki, *J. Phys. Chem. C* **2014**, *118*, 25809.
[37] S. Vantasin, Y. Tanaka, S. Uemura, T. Suzuki, Y. Kutsuma, D. Doujima, T. Kaneko, Y. Ozaki, *Phys. Chem. Chem. Phys.* **2015**, *17*, 28993.
[38] R. Beams, L. G. Cançado, A. Jorio, A. N. Vamivakas, L. Novotny, *Nanotechnology* **2010**, *26*, 75702.
[39] J. Rogalski, K. Braun, A. Horneber, M. van den Berg, J. Uihlein, H. Peisert, T. Chassé, A. J. Meixner, D. Zhang, *Vibrational Spectrosc.* **2017**, *91*, 128.
[40] K. Ikeda, M. Takase, N. Hayazawa, S. Kawata, K. Murakoshi, K. Uosaki, *J. Am. Chem. Soc* **2013**, *135*, 11489.
[41] M. Dyba, S. Hell, *Phys. Rev. Lett.* **2002**, *88*, 163901.
[42] E. Betzig, G. H. Patterson, R. Sougrat, O. W. Lindwasser, S. Olenych, J. S. Bonifacino, M. W. Davidson, J. Lippincott-Schwartz, H. F. Hess, *Science* **2006**, *313*, 1642.
[43] M. Rust, M. Bates, X. Zhuang, *Nature Methods* **2006**, *3*, 793.
[44] C. Cleff, P. Groß, C. Fallnich, H. L. Offerhaus, J. L. Herek, K. Kruse, W. P. Beeker, C. J. Lee, K.-J. Boller, *Phys. Rev. A* **2012**, *86*, 023825.
[45] C. Cleff, P. Groß, C. Fallnich, H. L. Offerhaus, J. L. Herek, K. Kruse, W. P. Beeker, C. J. Lee, K.-J. Boller, *Phys. Rev. A* **2013**, *87*, 033830.
[46] L. Gong, H. Wang, *Phys. Rev. A* **2014**, *90*, 013818.
[47] L. G. Cançado, R. Beams, A. Jorio, L. Novotny, *Phys. Rev. X* **2014**, *4*, 031054.
[48] L. Novotny, R. X. Bian, X. S. Xie, *Phys. Rev. Lett.* **1997**, *79*, 645.
[49] L. Novotny, S. J. Stranick, *Ann. Rev. Phys. Chem.* **2006**, *57*, 303.
[50] L. Novotny, B. Hecht, *Principles of Nano-optics*, Cambridge University Press, Cambridge, **2006**.
[51] L. G. Cançado, A. Jorio, A. Ismach, E. Joselevich, A. Hartschuh, L. Novotny, *Phys. Rev. Lett.* **2009**, *103*, 186101.
[52] R. Beams, D. Smith, T. W. Johnson, S.-H. Oh, L. Novotny, A. N. Vamivakas, *Nano Lett* **2013**, *13*, 3807.
[53] R. Beams, L. G. Cançado, S.-H. Oh, A. Jorio, L. Novotny, *Phys. Rev. Lett.* **2014**, *113*, 186101.
[54] W. Carter, E. Wolf, *J. Opt. Soc. Am.* **1975**, *65*, 1067.
[55] R. Carminati, J. J. Greffet, *Phys. Rev. Lett.* **1999**, *82*, 1660.
[56] A. V. Shchegrov, K. Joulain, R. Carminati, J.-J. Greffet, *Phys. Rev. Lett.* **2000**, *85*, 1548.
[57] H. Roychowdhury, E. Wolf, *Opt. Lett.* **2003**, *28*, 170.
[58] A. Apostol, A. Dogariu, *Phys. Rev. Lett.* **2003**, *91*, 093901.
[59] H. Roychowdhury, E. Wolf, *J. Mod. Opt.* **2004**, *51*, 1603.
[60] B. T. O'Callahan, W. E. Lewis, A. C. Jones, M. B. Raschke, *Phys. Rev. B* **2014**, *89*, 245446.
[61] R. V. Maximiano, R. Beams, L. Novotny, A. Jorio, L. G. Cançado, *Phys. Rev. B* **2012**, *85*, 235434.
[62] B. Latour, S. Volz, Y. Chalopin, *Phys. Rev. B* **2014**, *90*, 014307.
[63] J. Ribeiro-Soares, M. E. Oliveros, C. Garin, M. V. David, L. G. P. Martins, C. A. Almeida, E. H. Martins Ferreira, K. Takai, T. Enoki, R. Magalhaes-Paniago, A. Malachias, A. Jorio, B. S. Archanjo, C. A. Achete, *Carbon* **2015**, *95*, 646.
[64] L. G. Cançado, R. Beams, L. Novotny, **2008**. Preprint at <http://arxiv.org/abs/0802.3709> Access date February 2017.
[65] A. K. Gupta, T. J. Russin, H. R. Gutiérrez, P. C. Eklund, *ACS Nano* **2009**, *3*, 45.
[66] S. Neubeck, Y. M. You, Z. H. Ni, P. Blake, Z. X. Shen, A. K. Geim, K. S. Novoselov, *Appl. Phys. Lett.* **2010**, *97*, 053110.
[67] B. Krauss, P. Nemes-Incze, V. Skakalova, L. P. Biro, K. von Klitzing, J. H. Smet, *Nano Lett.* **2010**, *10*, 4544.
[68] Z. J. Lapin, R. Beams, L. G. Cançado, L. Novotny, *Faraday Discussions* **2015**, *184*, 193.
[69] A. J. Pollard, B. Brennan, H. Stec, B. J. Tyler, M. P. Seah, I. S. Gilmore, D. Roy, *Appl. Phys. Lett.* **2014**, *105*, 253107.
[70] A. Eckmann, A. Felten, A. Mishchenko, L. Britnell, R. Krupke, K. S. Novoselov, C. Casiraghi, *Nano Lett.* **2012**, *12*, 3925.
[71] C. Lee, X. Wei, J. W. Kysar, J. Hone, *Science* **2008**, *321*, 385.
[72] K. Elibol, B. C. Bayer, S. Hummel, J. Kotakoski, G. Argentero, J. C. Meyer, *Scientific Reports* **2016**, *6*, 28485.
[73] G. Verbiest, C. Stampfer, S. Huber, M. Andersen, K. Reuter, *Phys. Rev. B* **2016**, *93*, 195438.